



Article

High-Performance Porous pSi/Ag@C Anode for Lithium-Ion Batteries

Kefan Li ¹, Xiang Li ^{1,2,*} , Liang Yuan ¹, Zewen Han ¹, Mengkui Li ¹, Rui Ji ¹, Yixin Zhan ¹ and Kai Tang ^{3,*} ¹ School of Energy and Power Engineering, Jiangsu University, Zhenjiang 212013, China² Taizhou DongBo New Materials Co., Ltd., Taizhou 225312, China³ SINTEF Industry, N-7465 Trondheim, Norway

* Correspondence: xiangli@ujs.edu.cn (X.L.); kai.tang@sintef.no (K.T.)

Abstract: Silicon represents one of the most attractive anode materials in lithium-ion batteries (LIBs) due to its highest theoretical specific capacity. Thus, there is a most urgent need to prepare Si-based nano materials in a very efficient way and develop some reasonable approaches for their modification in order to resolve the short-falls of Si anodes, which include both low conductivity and huge volume changes during intercalation of lithium ions. In this work, the kerf loss silicon (KL Si) from the photovoltaic industry has been used as an inexpensive Si source for the preparation of a porous silicon/silver/carbon composite (pSi/Ag@C) as an anode material. Porous silicon was embedded with Ag particles via the Ag-catalyzed chemical etching process, providing additional space to accommodate the large volume expansion of silicon. After carbon coating from polymerization of tannic acid on the surface of pSi/Ag, a high-speed conductive network over the surface of silicon was built and contributed to enhancing the electrochemical performance of the anode. The pSi/Ag@C electrode discharge capacity maintained at a stable value of 665.3 mAh g⁻¹ after 100 cycles under 0.5 A g⁻¹ and exhibited good rate performance. Therefore, this study recommends that the method is very promising for producing a silicon anode material for LIBs from KL Si.

Keywords: kerf loss silicon; silver particles; anode; pSi/Ag@C composite



Citation: Li, K.; Li, X.; Yuan, L.; Han, Z.; Li, M.; Ji, R.; Zhan, Y.; Tang, K. High-Performance Porous pSi/Ag@C Anode for Lithium-Ion Batteries. *Processes* **2024**, *12*, 1021. <https://doi.org/10.3390/pr12051021>

Academic Editor: Gustavo M. Morales

Received: 29 April 2024

Revised: 12 May 2024

Accepted: 15 May 2024

Published: 17 May 2024



Copyright: © 2024 by the authors. Licensee MDPI, Basel, Switzerland. This article is an open access article distributed under the terms and conditions of the Creative Commons Attribution (CC BY) license (<https://creativecommons.org/licenses/by/4.0/>).

1. Introduction

Lithium-ion batteries (LIBs) are applied in a variety of fields and are seeking new anode materials with higher energy densities to substitute commercial graphite anodes [1]. Silicon-based anodes hold tremendous potential for next-generation LIBs [2]. They offer an exceptionally high theoretical charge capacity and a low lithiation voltage platform. Nevertheless, silicon anodes must overcome significant challenges to be widely used commercially. These include extremely low intrinsic electrical conductivity and drastic volume change (up to 300%) in the lithiation/delithiation process, resulting in a poor cycling stability [3,4].

To address these bottlenecks, researchers have focused on a wide range of strategies to enhance the electrochemical performance of silicon-based anodes. For instance, silicon nanoparticles [5], silicon nanowires [6], silicon nanosheets [7,8], silicon nanotubes [9], etc., can effectively mitigate the bulk effect of silicon. Preparation of Si@C composites as anode electrodes is also an effective method. CNTs [10,11] and graphite [12,13] are introduced as conductive carbon matrices to improve the conductivity of materials. Employing organic compounds like PDA [14,15], PAN [16,17], chitosan [18], glucose [10,19], and others as carbon forerunners to develop Si@C composites, either in core-shell or egg-yolk configurations, enhances the material's structural resilience.

Metallic materials are usually compounded with silicon due to their high electrical conductivity and high mechanical stability. Ensafi et al. [20] deposited Ni and Bi nanoparticles on the surface of porous silicon by magnesium thermal reduction, and Yu et al. [21] reported a Ag-coated 3D macroporous Si anode material prepared by Ag mirror reaction.

The metal coating existed as a tough shell to buffer the volume expansion of silicon during the lithiation process. However, the mass ratio of coating metals is too high and reduces the overall capacity of electrodes. Porous silicon allows room for its own volume expansion, and its interconnecting channels ensure efficient electrolyte penetration and shorten ionic transport paths [22,23]. However, the capacity degrades after a long cycling time owing to the intimate connection between nanostructures and electrolytes. In addition, ball milling [24,25], template method [26], resin curing [27], etc., were used to introduce carbon layers on the surface of Si/metal to solve the above problem. However, most synthesis approaches involve a complex preparation process, harsh reaction conditions or expensive raw materials, which prevent the application of Si/metal/C composites as commercial anodes.

This study utilizes kerf loss silicon (KL-Si) from the photovoltaic industry as a low-cost silicon source to synthesize high-performance anode materials. The photovoltaic industry has grown rapidly in the last decade, where high-purity silicon plays a vital role. During the production of silicon wafers by the diamond-wire sawing (DWS) process, there is about 30% of silicon that is wasted as kerf losses (KLs) of submicron- and micron-order powder [28,29]. The total amount of KL powder waste from the global photovoltaic industry is estimated at around 4×10^5 tons in 2022 [30,31]. This results in increased growing environmental pollution and the waste of high-purity Si resources.

In this study, firstly, KL Si was nanosized through ball milling and purified using acid pickling to produce nanoscale Si powder. Ag-assisted chemical etching allows Ag particles to enter the silicon interior to obtain pSi/Ag, and the Ag particles improve the electrical conductivity of silicon. Porous silicon/silver/carbon composite (pSi/Ag@C) was formed by tannic acid self-polymerization on the surface of pSi/Ag and carbonization subsequently. A high-speed conductive network over the surface of silicon was built and enhanced the stability and electrochemical properties of the silicon-based anode. This research offers a method to recycle KL Si waste effectively, mitigating resource depletion and environmental harm, while also presenting a viable approach to crafting superior anode materials for LIBs.

2. Experimental

2.1. Raw Materials

Silver nitrate solution (AgNO_3 , AR), hydrochloric acid (HCl, AR), Ethanol, hydrofluoric acid (HF, AR), hydrogen peroxide (H_2O_2 , AR), hydroxymethyl aminomethane (Tris, AR), carboxyl methyl cellulose (CMC, AR), all of analytical grade, were supplied from Shanghai Macklin Biochemical Co., Ltd. (Shanghai, China). Argon (99.999%) was delivered by Zhongpu Gas Co., Ltd. (Zhenjiang, China).

2.2. Synthesis of pSi/Ag@C

The synthesis procedure of the pSi/Ag@C composite is shown in Figure 1. Purified silicon nanoparticles (Si NPs) were produced by wet ball milling and picking of the KL Si, as detailed in our previous study [32].

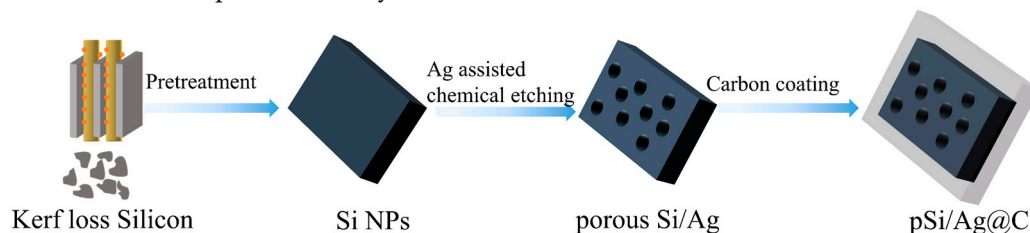


Figure 1. The synthetic processes of the pSi/Ag@C composite.

Firstly, 200 mg Si NPs were added to 30 mL of deionized water and ultrasonically dispersed for 10 min, followed by adding 16 mL of ethanol, 10 mL of HF (4.6 mol/L), 2 mL H_2O_2 (0.1 mol/L), and 1 mL of AgNO_3 (0.1 mol/L). Then, the solution was stirred for 1 h in the dark room. The dark room prevents the irreversible photoreduction of AgNO_3 at low

concentrations in solution under light, which was created by covering the beaker with a black box. After centrifugation at 4000 rpm for 10 min, the pSi/Ag precipitate was obtained and washed with deionized water until the supernatant was neutral.

Secondly, 100 mg pSi/Ag was added into 50 mL of Tris buffer (0.1 mol/L, PH = 7.0), followed by ultrasonic dispersion for 0.5 h. After that, 100 mg tannic acid was added and stirred for 24 h. The precipitate obtained by centrifugation was washed several times using deionized water until the supernatant was colorless. Then, the precipitate was transferred to an oven at 70 °C for 12 h.

Finally, the dried powder was calcined in a tube furnace under argon atmosphere. The furnace temperature was raised to 400 °C with a rate of 3 °C/min and was maintained for 2 h, and then it was raised to 800 °C with a rate of 5 °C/min for 2 h. The obtained sample was named as pSi/Ag@C. By contrast, the Si@C composite was also prepared by the above procedure without Ag doping.

2.3. Characteristic Analysis

The particle size of samples was tested with a Laser Particle Sizer (Mastersizer 3000, Malvern, UK). The morphologies of the samples were examined by SEM (Hitachi S-3500N, Ibaraki, Japan) operated at 20 KV and by TEM (HT7800, Ibaraki, Japan) under 120 KV. The crystal phase of the samples was characterized by XRD (D8 ADVANCE, Burker, Karlsruhe, Germany) with a Cu K α radiation source ($\lambda = 1.5418 \text{ \AA}$) at a step of $0.05^\circ \text{ s}^{-1}$. The specific surface area and pore size distribution of the samples were measured by ASAP2460 (Micromeritics, Norcross, GA, USA). The crystallinity of the composites was determined by Raman spectroscopy (DXR3, ThermoFisher, Waltham, MA, USA) with a 532 nm laser. Thermal gravimetric (TG) testing was carried out in an air atmosphere (NETZSCH STA449F3, Jupiter, Selb, Germany). X-ray photoelectron spectroscopy (XPS), employing a monochromatic Al K α radiation source (ESCALAB QXi, Thermo Scientific, Waltham, MA, USA), was used to characterize the surface composition of the samples.

2.4. Electrochemical Measurements

The working electrode slurries were produced by mixing 80 wt% active materials, 10 wt% carboxymethyl cellulose and 10 wt% super P in deionized water. The blended slurry was cast in the pure copper foil collector at a thickness of 150 μm , and the drying process was carried out in an oven at 80 °C for 12 h. Next, the electrode was carefully cut into sheets with a diameter of 12 mm using a specialized hole punch, and the loading mass of the active material in the electrodes was about 1.1 mg cm^2 . The produced working electrode were assembled into the CR2032 half cells in a glove box. Pure Li metal foil was used as the counter electrode, while a porous polypropylene membrane (Celgard 2500) was used as the separator. The LiPF₆ was used as an electrolyte, consisting of ethylene carbonate and diethyl ethyl carbonate (1:1 in volume), with 5 wt% of fluorinated ethylene carbonate.

The galvanostatic charge–discharge (GCD) measurements and rate performance tests were performed using the Neware 4008T test system (Neware Technology Limited, Shenzhen, China) in the voltage range of 0.01–1.2 V. Electrochemical analyses were performed on Ivium–n–Stat electrochemical workstation (Ivium Technologies BV, Eindhoven, Netherlands). Cyclic voltammetry (CV) tests were conducted with a scan rate of 0.1 mV/s. Electrochemical impedance spectroscopy (EIS) analyses were performed over a frequency range of 100 kHz to 0.01 Hz.

3. Results and Discussion

The KL Si collected from DWS operations in the PV industry consists of particles sized at the micron and submicron level, as well as abundant organic and inorganic impurities. Pure nanosized Si NPs were obtained by pretreatment of KL Si, including ball milling, acid pickling and calcination, representing an inexpensive silicon source for the synthesis of anode. The metallic impurities in KL Si had been effectively removed, as detailed in our previous study [32]. Laser particle size analysis (Figure 2) revealed a significant reduction

in average particle size from 1246.8 nm for KL Si to 262.1 nm for Si NPs. Si NPs and Ag^+ spontaneously form a galvanic cell system during the chemical etching process, where Si NPs as the anode lose electrons and Ag^+ forces electrons to be reduced to Ag particles at the cathode. As the corrosion reaction by HF and H_2O_2 continued, the Si near the Ag particles was oxidized and subsequently dissolved to form a porous structure, and Ag particles were embedded inside the holes [33]. The pSi/Ag composite was obtained through the above Ag-catalyzed chemical etching process. An organic coating on the surface of pSi/Ag was obtained by the self-polymerization of tannic acid [34] and transformed into a carbon layer after high temperature carbonization to complete the pSi/Ag@C composite.

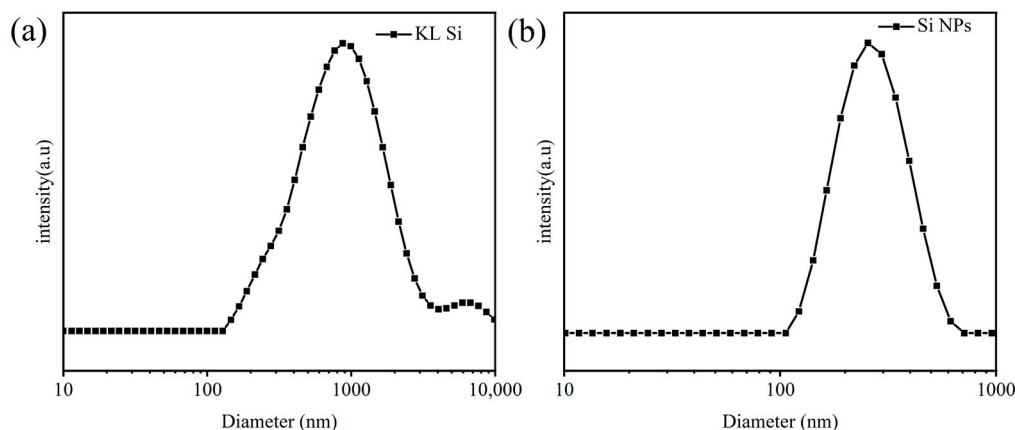


Figure 2. Particle size distribution of (a) KL Si waste and (b) Si NPs.

The metal-assisted chemical etching (MACE) method was reported in many studies to embed metal nanoparticles into silicon to construct porous structures, where Ag, Au, Pt and Pd are the most frequently used [35–37]. In the case of less noble metals such as Ni and Co, due to the fact that the redox potential of these metals is negative, hydrogen evolution dominates over the metal displacement. So, the fluoride solution at pH 8 must be used for metal deposition on the silicon surface, which is difficult to control [38]. The Ag has superior electrical conductivity to less noble metals and is much cheaper than Au, Pt and Pd. In addition, the use of Ag is very limited in the etching process. Therefore, Ag was the best candidate for metal-assisted chemical etching of Si as an anode material.

SEM characterization revealed the morphology of the samples, as shown in Figure 3. KL Si (Figure 3a) consists of irregular large flakes of microns and submicron size. In contrast, Si NPs (Figure 3b) obtained by pretreatment of KL Si exhibit significantly reduced particle size. For the pSi/Ag composite, abundant macro pores on the silicon particles' surface can be clearly observed from Figure 3c, which were formed by the Ag-assisted chemical etching and widened the space to alleviate the volume expansion of silicon particles in the process of Li^+ embedding. The surface of the pSi/Ag@C composite shown in Figure 3d was much smoother after coating of the carbon layer and the pore size was significantly reduced compared to pSi/Ag. The elemental mapping of pSi/Ag@C was performed and is shown in Figure 3e. The Ag particles were distributed in the Si matrix with agglomeration in the etched pores. The uniform presence of the C element indicates the well-coated carbon layer on the surface of the Si particles. The EDS mapping results reveal that the Ag content in the composite is approximately 3.3 wt%. Figure 3f,g show the TEM images of the pSi/Ag@C composite at different magnifications. As shown in Figure 3f, pSi/Ag@C particles embedded with many small Ag particles can be observed. Figure 3g displays the high magnification TEM image, which provides more details about the structure of the pSi/Ag@C composite. The results show that the Ag particles with a size less than 100 nm were uniformly embedded into the Si particles, and pSi/Ag particles were coated with a carbon layer with a thickness of approximately 15 nm (marked in the yellow dash line zone in Figure 3g), which was generated by carbonization of the tannic acid polymer.

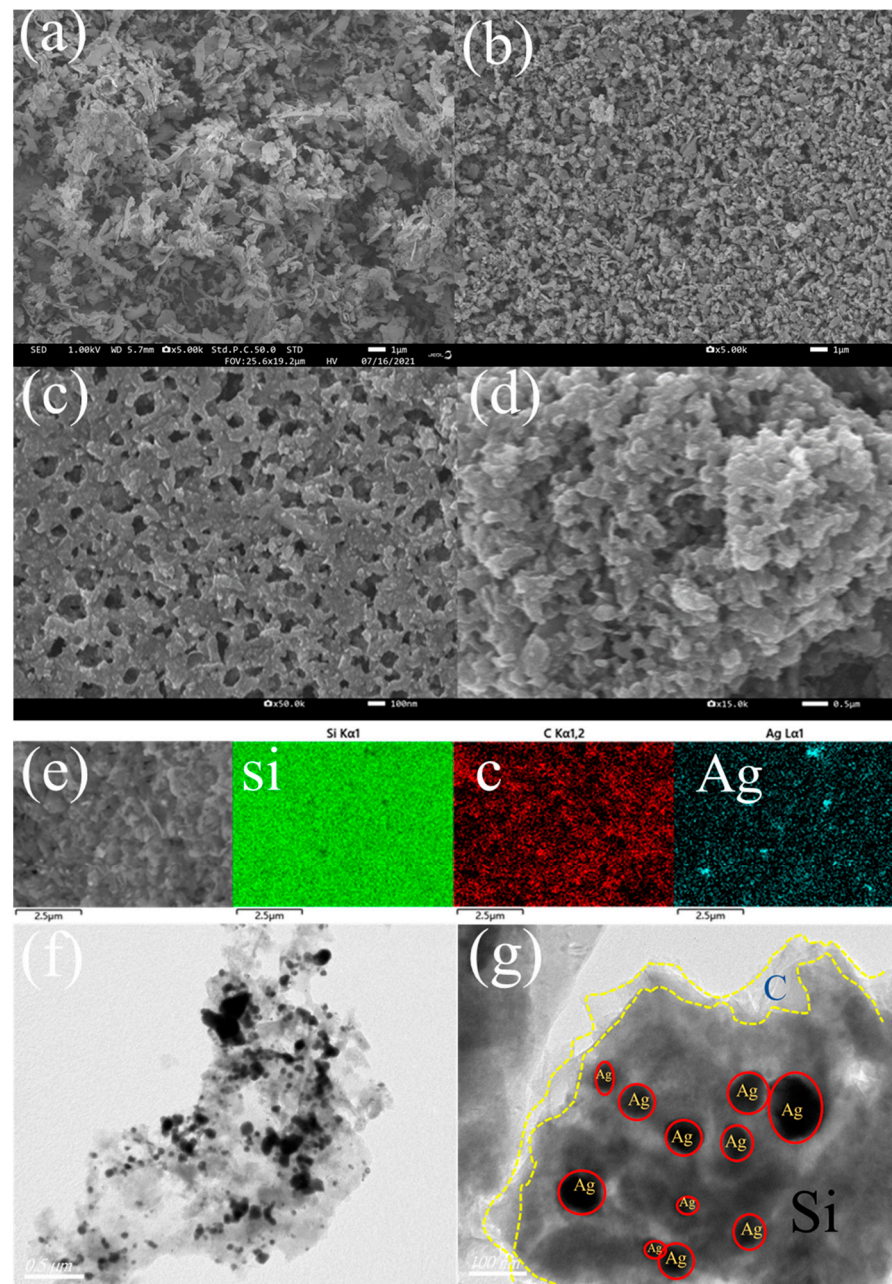


Figure 3. SEM image of KL Si (a), Si NPs (b), pSi/Ag (c) and pSi/Ag@C (d); elemental mapping of pSi/Ag@C (e); (f,g) TEM image of pSi/Ag@C.

Figure 4a presents XRD patterns of pSi/Ag@C, pSi/Ag and Si NPs. Characteristic peaks of all three samples appear at 28.5° , 47.4° , 56.2° , 69.2° and 76.4° , fitting to the (111), (220), (311), (400) and (311) crystal planes of crystalline silicon (JCPDS 05-0565), respectively. The kerf loss silicon (KL Si) was recycled from a silicon wafer produced by diamond-wire sawing of a silicon ingot, which is crystalline silicon. Si NPs were obtained by pretreatment of KL Si, including ball milling, acid pickling and calcination, but their crystal structure was not changed. The pSi/Ag@C composite was synthesized using Si NPs as a silicon source, still remaining in the crystalline Si phase. The XRD analysis demonstrates that Ag-assisted chemical etching and carbon coating processes do not change the crystal structure of Si NPs. In the patterns of pSi/Ag@C and pSi/Ag, characteristic peaks at 38.2° , 44.1° , 64.3° and 77.4° fit to the (111), (200), (220) and (331) crystal planes of crystalline Ag (JCPDS 04-0783). This indicates that the Ag-assisted chemical etching process did not change the crystal structure

of silicon and the silver exhibited good crystallinity. The absence of carbon peaks indicates that the formed carbon layer mainly consists of amorphous carbon [39]. Further analysis of the carbon phase present in the composites was performed by Raman spectrum and is shown in Figure 4b. All samples exhibit typical peaks of silicon at 490 cm^{-1} and 915 cm^{-1} , while pSi/Ag@C exhibits peaks at 1365.7 cm^{-1} and 1583.6 cm^{-1} , corresponding to defect vibrations (D-band) and carbon atom sp^2 hybridized vibration (G-band), respectively. The I_D/I_G value is 0.96 for pSi/Ag@C, indicating a low level of graphitization, which is in agreement with XRD patterns. This defective carbon layer provides isotropic Li^+ transport pathways and more lithiation/delithiation active sites.

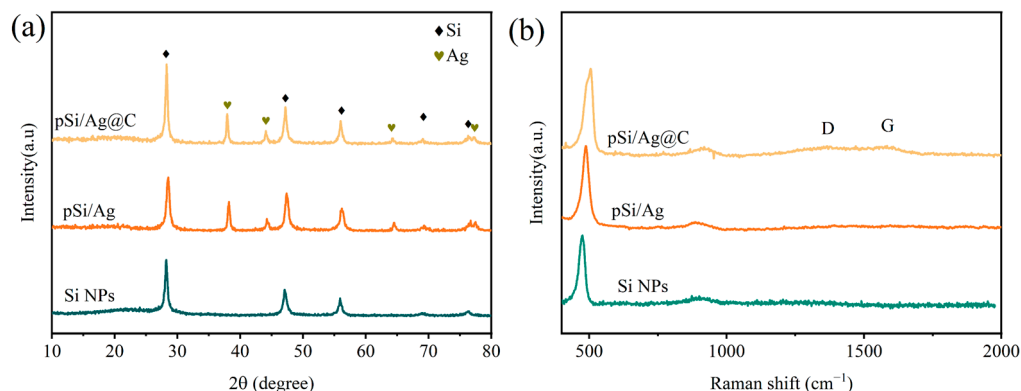


Figure 4. (a) XRD patterns; (b) Raman spectrum of Si NPs, pSi/Ag and pSi/Ag@C.

The determination of the carbon content of pSi/Ag@C composite was carried out using TG operated in the air atmosphere, and the obtained TG plots are presented in Figure 5. The pSi/Ag@C sample has two main weight loss events. The first weight loss, about 2.1 wt% below $100\text{ }^{\circ}\text{C}$, is assigned to the desorption of physically adsorbed H_2O . The second weight loss, occurring in the temperature range of $300\text{--}600\text{ }^{\circ}\text{C}$, is mainly assigned to the oxidation of carbon, which is approximately 15.9 wt%. It should be noted that the oxidation of silicon at temperatures above $550\text{ }^{\circ}\text{C}$ leads to a slight increase in weight (1.6 wt%), as shown in the TG plot of Si NPs. Therefore, the carbon content of pSi/Ag@C was evaluated to be 14.6 wt%, which has been corrected in consideration of the oxidation of silicon (approximately 80 wt% in pSi/Ag@C composite).

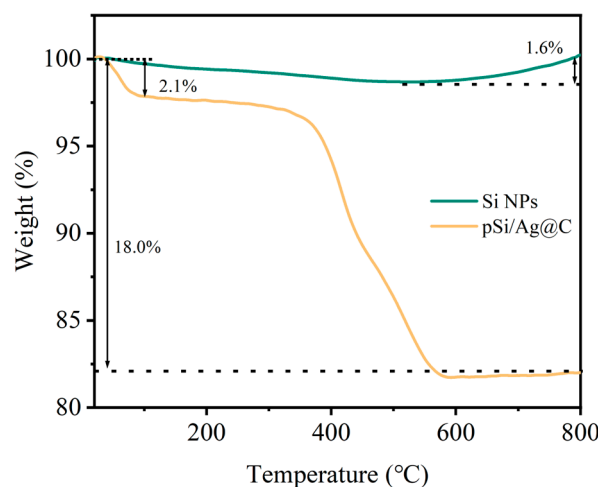


Figure 5. TG plots of Si NPs and pSi/Ag@C.

Figure 6a presents the N_2 adsorption–desorption isotherms of Si NPs, pSi/Ag and pSi/Ag@C composites, where Si NPs exhibit a typical II isotherm (IUPAC classification),

and pSi/Ag and pSi/Ag@C exhibit a typical IV-type isotherm with hysteresis loops, indicating the presence of mesopores. The BET-specific surface areas of Si NPs, pSi/Ag and pSi/Ag@C composites are 24.2, 82.6 and 8.9 $\text{m}^2 \text{g}^{-1}$, respectively. And the pore volume of the above three samples is 0.11, 0.31, and 0.04 $\text{cm}^3 \text{g}^{-1}$, respectively. Due to the Ag-assisted chemical etching of Si particles, an increase in porosity leads to an enlarged specific surface area and pore volume of the pSi/Ag composite. The specific surface area and pore volume of pSi/Ag@C is decreased due to the blocking of the partial macroporous structure by the coated carbon. The BJH pore size distribution of Si NPs (Figure 6b) shows a broad distribution in the range of 10–100 nm, which is probably the intergranular space between the Si nanoparticles. After Ag-assisted chemical etching of Si NPs, pSi/Ag reveals a much richer meso and macroporous structure. The macroporous porosity of pSi/Ag@C decreased significantly after carbon coating. The results are consistent with the SEM images shown in Figure 3.

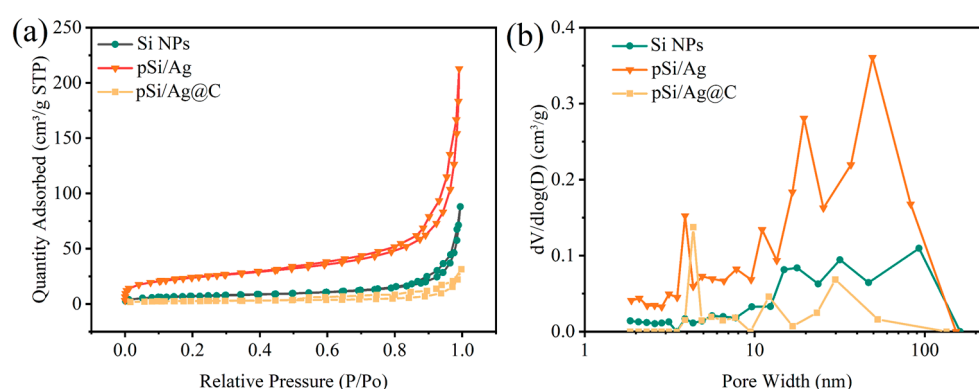


Figure 6. (a) N_2 adsorption–desorption isotherms; (b) BJH pore size distribution of Si NPs, pSi/Ag and pSi/Ag@C.

XPS analysis of pSi/Ag@C composite (Figure 7a) reveals characteristic peaks for Si 2p, C 1s, O 1s and Ag 3d in the survey scanning spectrum. In the high-resolution Si 2p spectrum (Figure 7b), the peaks at 98.1 and 98.6 eV correspond to Si 2p_{3/2} and Si 2p_{2/1}, and the peak at 102.4 eV corresponds to the Si-O-Si bond of SiO_x [40]. The strong Si-O-Si peak is due to the oxidation of Si, which may have occurred during wet ball milling of KL Si waste. The further oxidization of Si particle is very slow and difficult due to the restricted O diffusion through the amorphous oxide layer [41]. The generated oxide layer enhances the electrode's cyclic stability by limiting the volume expansion of Si [42]. In Figure 7d, the C 1s spectrum can be deconvoluted into peaks of C-O-Si (288.1 eV), C-C (284.5 eV) and C=C (283.1 eV), respectively [42]. The Ag 3d spectrum (Figure 7c) exhibits two peaks with a spacing of 6 eV, located at 366.9 eV and 372.9 eV corresponding to Ag^0 3d_{5/2} and Ag^0 3d_{3/2}, respectively, demonstrating the high crystallization of Ag^0 [43].

The CV curves of the pSi/Ag and pSi/Ag@C electrode for the first three cycles are shown in Figure 8a,b, respectively. During the first cathodic scan, a wide cathodic peak appears at 0.79 V in pSi/Ag and 0.61 V in pSi/Ag@C, which is related to the generation of the SEI layer [44]. The reduction peak for both electrodes appears at approximately 0.2 V, which can be attributed to the transformation from the crystalline silicon to the amorphous Li_xSi alloy in the first cathodic scan. In the oxidation curve, the two peaks of 0.31 V and 0.53 V are due to the decay of amorphous Li_xSi and back to crystal Si [45]. With an increase in the number of scans, the activation kinetics of the material gradually improve, and the peak current of all peaks increases correspondingly [46]. These two electrodes exhibit anodic and cathodic peaks at similar positions and point to the lithiation transition associated with silicon; all the curves do not show peaks due to the reaction between Ag and Li, which indicates that the Ag particles do not change the lithiation behavior of pSi/Ag and pSi/Ag@C electrodes. In addition, the higher peak current of pSi/Ag@C during the test implies that it has superior electrochemical reaction kinetics.

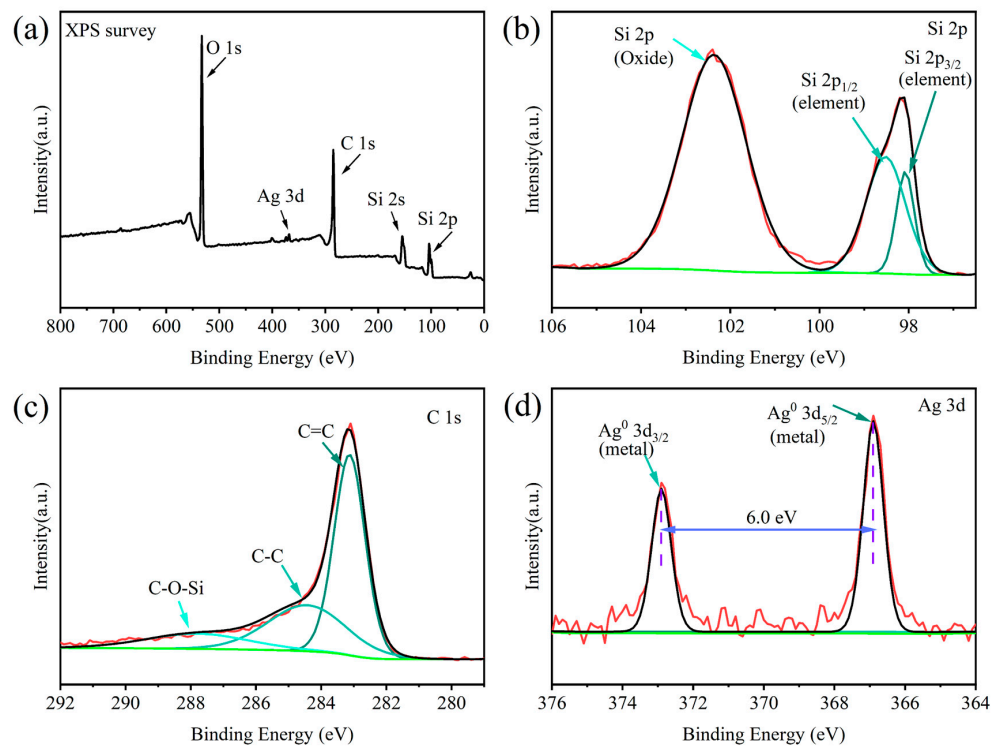


Figure 7. XPS spectra of pSi/Ag@C: (a) survey scanning spectrum, (b) Si 2p, (c) C 1s, (d) Ag 3d.

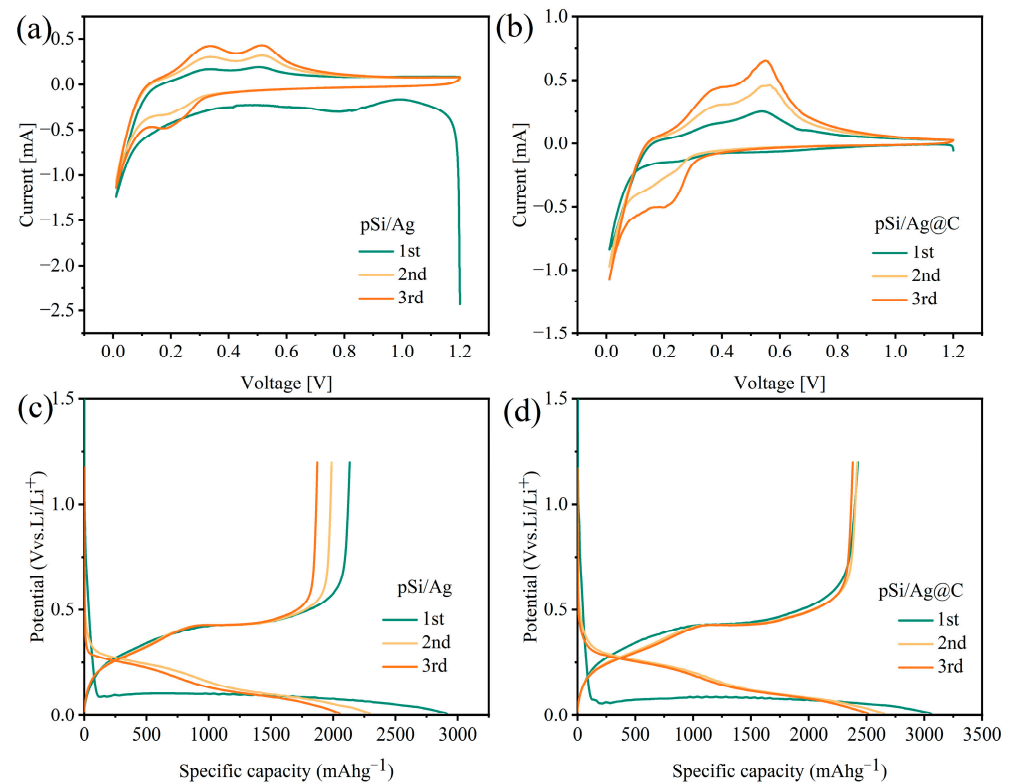


Figure 8. CV curves for the premier three cycles of (a) pSi/Ag electrode and (b) pSi/Ag@C electrode; GCD curves for the premier three cycles at 0.1 A g⁻¹ of (c) pSi/Ag electrode and (d) pSi/Ag@C electrode.

GCD curves of pSi/Ag and pSi/Ag@C electrodes for the first three cycles under 0.1 A g⁻¹ presented in Figure 8c,d, respectively. Both of them show charging plateaus (0.2–0.5 V) and discharging plateaus (0.25–0.01 V). The initial discharge/charge capacities

of the pSi/Ag and pSi/Ag@C electrodes 2912.1/2132.6 and 3058.5/2426.1 mAh g⁻¹, respectively, with corresponding initial coulombic efficiencies (ICE) of 73.2% and 79.3%. The coulombic efficiencies (CE) of the second and third cycle for pSi/Ag@C electrodes is 90.1% and 94.5%, respectively. The pSi/Ag@C electrode generates a stable SEI film more quickly during charge–discharge cycles, indicating its better performance regarding Li⁺ reversible storage.

Figure 9a shows the rate capabilities of Si NPs, Si@C, pSi/Ag and pSi/Ag@C electrodes. The specific capacity of the pSi/Ag@C electrode is 2369.5, 2015.1, 1635.7 and 1033.8 mAh g⁻¹ after five cycles under 0.1, 0.25, 0.5 and 1.0 A g⁻¹, respectively. The specific capacity recovered to the original level (1958.7 mAh g⁻¹) when the current was restored to 0.1 A g⁻¹, showing a stable rate performance. The specific capacities of Si NPs, Si@C and pSi/Ag electrodes after current restoration are 116.1, 1352.3 and 1060.7 mAh g⁻¹, respectively, much lower than their 3106.1, 2343.4 and 2912.1 mAh g⁻¹ initial specific capacities.

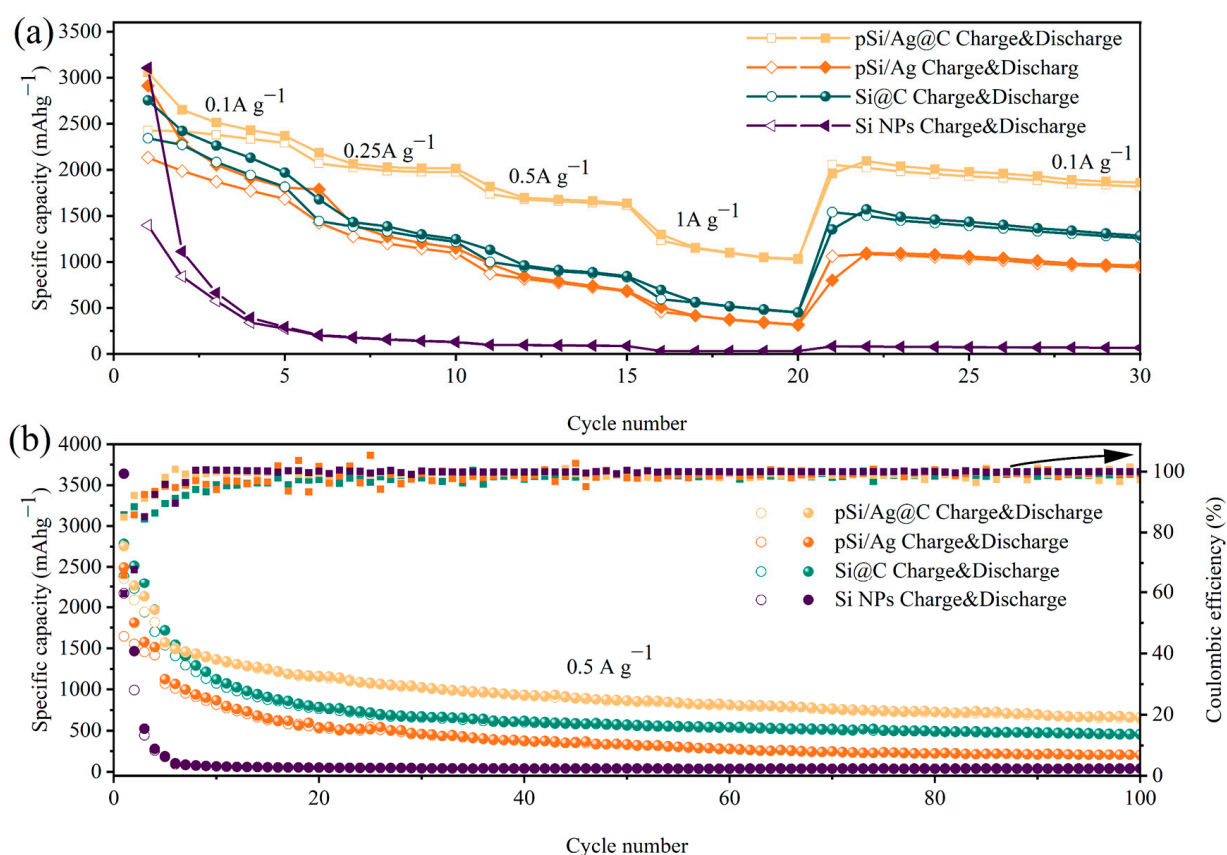


Figure 9. (a) Rate performance of electrodes; (b) cycle performance of electrodes at 0.5 A g⁻¹.

Figure 9b presents a contrast in the cycling stability of Si NPs, Si@C, pSi/Ag and pSi/Ag@C electrodes under 0.5 A g⁻¹. The Si NP electrode shows dramatic capacity fading in the first ten cycles, as expected. The specific capacity of the pSi/Ag and pSi/Ag@C electrode remained at 204.5 and 457.4 mAh g⁻¹ after 100 cycles, respectively. The pSi/Ag@C electrode remained at the highest capacity of 665.3 mAh g⁻¹ after 100 cycles. Both of the electrochemical performances of pSi/Ag with a porous structure and Si@C with a carbon coating are improved compared to Si NPs. And the combination of the porous structure and carbon coating further improves the rate and cycle performance of the electrode. Compared with recently reported anode materials based on KL Si waste (Table 1), the pSi/Ag@C electrode also exhibits superior electrochemical performance.

Table 1. Contrast of the recent work based on KL Si waste as anodes for LIBs.

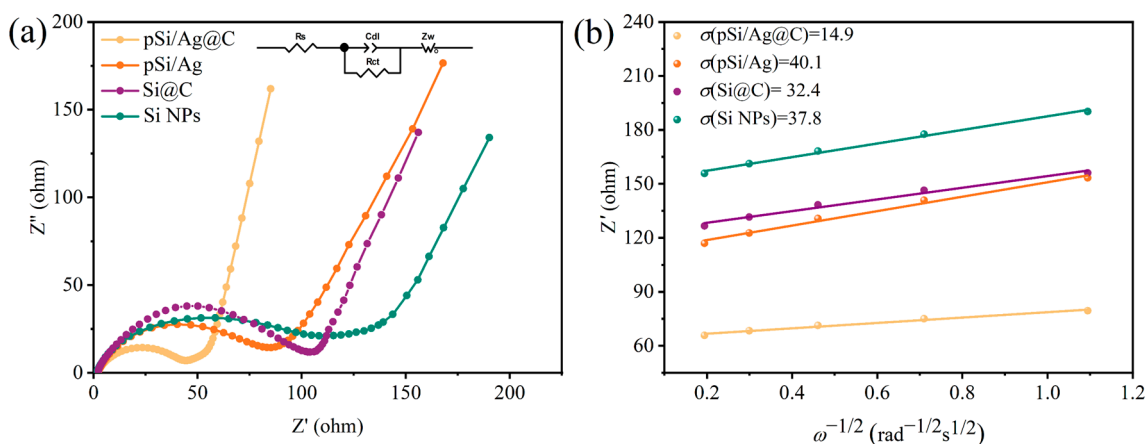
Electrode Material	Voltage Range	Current Density	Cycling Stability [mAh g ⁻¹] (Cycle)	Refs
3P-2h	0.01–2.0 V	0.05 A g ⁻¹	636 mAh g ⁻¹ (50th)	[47]
Si@Cppy	0.01–1.5 V	0.1 A g ⁻¹	335 mAh g ⁻¹ (200th)	[48]
GF-Si-C30/Si	0.01–1.5 V	0.5 A g ⁻¹	501 mAh g ⁻¹ (150th)	[49]
GPSCM20-900-C	0.01–2.0 V	0.05 A g ⁻¹	560 mAh g ⁻¹ (50th)	[50]
Si/PA-C(1:6)	0.01–2.5 V	0.1 A g ⁻¹	317.7 mAh g ⁻¹ (100th)	[51]
P-Si/C	0.01–2.0 V	0.05 A g ⁻¹	520 mAh g ⁻¹ (100th)	[52]
N-Si	0.01–1.5 V	0.42 A g ⁻¹	600 mAh g ⁻¹ (200th)	[53]
Si/TiSi ₂	0.01–1.5 V	0.5 A g ⁻¹	555 mAh g ⁻¹ (200th)	[54]
pSi/Ag@C	0.01–1.2 V	0.5 A g ⁻¹	665.3 mAh g ⁻¹ (150th)	present work

Figure 10a displays EIS curves of the pristine electrodes. Analysis reveals that the high-frequency semicircle signifies charge-transfer resistance (R_{ct}), and the straight line at low-frequency indicates electrolyte resistance (R_s) [55]. Using an equivalent circuit model, the R_{ct} value of pSi/Ag@C (44.3 Ω), pSi/Ag (85.6 Ω) and Si@C (104.4 Ω) is determined to be significantly lower than that of Si NPs (115.3 Ω). This demonstrates notably enhanced charge transfer kinetics for the pSi/Ag@C, pSi/Ag and Si@C electrode. pSi/Ag@C has the smallest R_{ct} value, mainly due to the introduction of Ag nanoparticles and the porous structure, indicating higher lithium-ion transfer rate. The diffusion coefficient of Li^+ can be evaluated by the following Equations (1) and (2) [56]:

$$Z' = R_e + R_{ct} + \sigma\omega^{-0.5} \quad (1)$$

$$D_{\text{Li}^+} = \frac{R^2 T^2}{2A^2 n^4 F^4 C^2 \sigma^2} \quad (2)$$

where σ represents the Warburg factor, ω represents the angular frequency, R represents the gas constant, T represents the temperature, A represents the surface area of the electrode, n represents the transfer electron number, F represents the Faraday constant, and lithium ions' concentration is represented by C . The value of σ is determined by the slope of the fitting line of Z' to $\omega^{-0.5}$, as depicted in Figure 10b. The calculated σ values for Si NPs, Si@C, pSi/Ag and pSi/Ag@C electrode is 37.8, 32.4, 40.1 and 14.9 $\Omega \text{ cm}^2 \text{ s}^{-0.5}$ separately. The D_{Li^+} of pSi/Ag@C anode is about 7.2 times that of Si NPs.

**Figure 10.** (a) Nyquist plots of Si NPs, Si@C, pSi/Ag and pSi/Ag@C electrodes; (b) relationship between Z' and $\omega^{-1/2}$ for Si NPs, Si@C, pSi/Ag and pSi/Ag@C electrode.

The electrochemical kinetic of the presented electrodes was further studied by measuring the CV curves at different scan rates from 0.25 to 1 mV s^{-1} . The results can be viewed

in Figures 11a, 11d and 11g for the pSi/Ag@C, Si@C, and Si NP electrode, respectively. The CV curves of the pSi/Ag@C electrode show similar oxidation–reduction peaks, indicating excellent reversibility. The relationship between peak current (i) and scan rate (v) is typically described by $i = av^b$, where a and b are adjustable parameters. The b is 0.5 indicates that Li^+ ion storage is primarily controlled by diffusion, while a b value of 1 implies predominantly capacitive behavior [57]. The line fittings of $\log(i)$ and $\log(v)$ are presented in Figure 11b, e and h to calculate the b values, where the pSi/Ag@C, Si@C, and Si NP electrode has a b value of 0.62, 0.56 and 0.28, respectively. The calculated results suggest that the electrochemical reaction kinetics of the pSi/Ag@C electrode are jointly controlled by pseudocapacitance and diffusion reactions. Moreover, the percentage of capacitive and diffusion contribution is determined by Equation (3):

$$i(V) = k_1v + k_2v^{0.5} \quad (3)$$

where $i(V)$, k_1v and $k_2v^{0.5}$ represent voltage, the capacitance contribution and the diffusion contribution, respectively [58]. As depicted in Figure 11c, the capacitive contribution of the pSi/Ag@C electrode increased from 45% to 62% with a scan rate from 0.25 to 1 mV s^{-1} . Compared to the Si@C and Si NP electrodes (Figure 11f,i), pSi/Ag@C demonstrates the highest capacitive contributions across various scan rates. This is likely due to the porous structure of pSi/Ag@C providing additional active sites, and its high-speed conductive network promotes the transport of Li^+ , which remains stable and of high capacity at high currents [59].

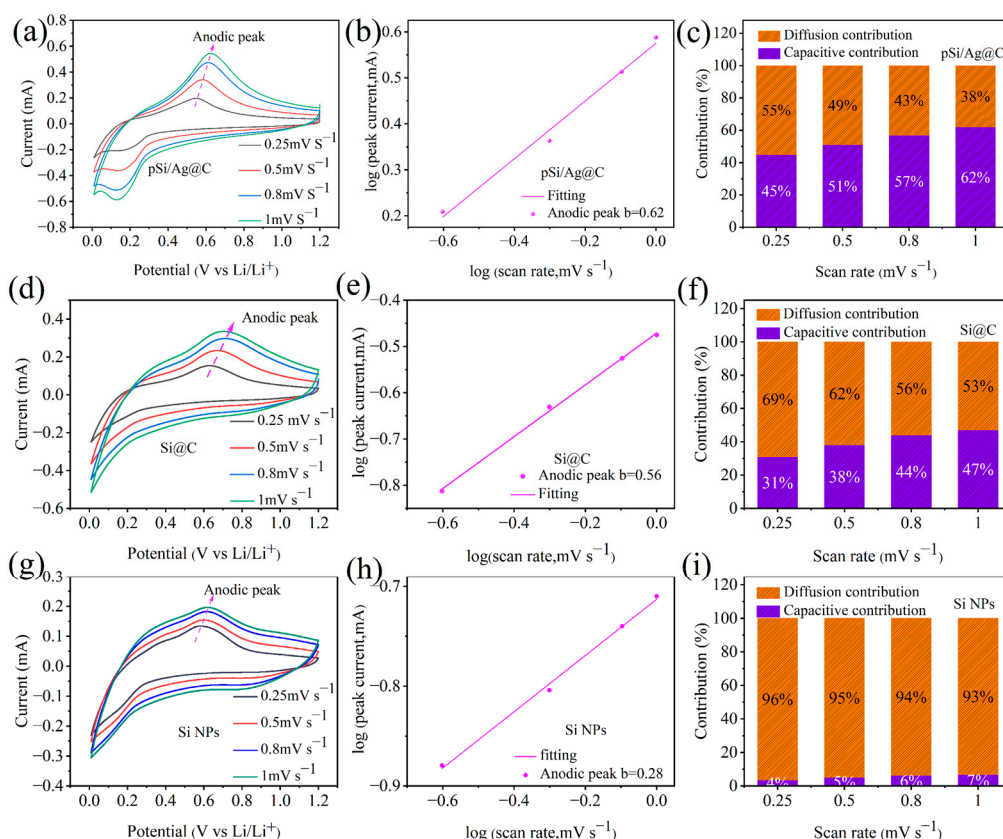


Figure 11. (a,d,g) CV curves of pSi/Ag@C, Si@C and Si NP electrodes at varying scan rates; (b,e,h) line fitting of $\log(i)$ and $\log(v)$ for pSi/Ag@C, Si@C, and Si NP electrodes; (c,f,i) capacitive and diffusion contributions for pSi/Ag@C, Si@C, and Si NP electrodes.

4. Conclusions

The pSi/Ag@C configuration as anode materials for LIBs was successfully synthesized using KL Si waste through Ag-catalyzed chemical etching and, subsequently, coating of

carbon. The rich porous structure obtained from chemical etching accommodates the volume change of silicon during charge/discharge cycles and shortens the Li^+ transport path. A high-speed conductive network made up of the doping Ag and the carbon layer improves the conductivity of the electrode significantly and also prevents direct interaction between the electrolyte and silicon particles. Ultimately, the pSi/Ag@C electrode exhibits excellent rate performance, with capacities of 2369.5, 2015.1, 1635.7 and 1033.8 mAh g^{-1} under 0.1, 0.25, 0.5 and 1.0 A g^{-1} , respectively. The pSi/Ag@C electrode also shows prominent stability with 665.3 mAh g^{-1} after 100 cycles at 0.5 A g^{-1} and an ICE of 79.3%. This approach not only provides a practical and feasible industrial production method for the effective recycling and utilization of waste silicon from the photovoltaic industry but also offers an inexpensive solution for industrial applications of silicon anode.

Author Contributions: Conceptualization, K.L. and L.Y.; methodology, K.L.; formal analysis, K.L. and Z.H.; investigation, M.L., Y.Z. and R.J.; writing—original draft preparation, X.L. and K.L.; writing—review and editing, X.L. and K.T.; supervision, X.L. and K.T.; funding acquisition, X.L. All authors have read and agreed to the published version of the manuscript.

Funding: The study was sponsored by the Taizhou Science and Technology Bureau (TS202202), Department of Human Resources and Social Security of Jiangsu Province (2021K180B), and Jiangsu University (18JDG015).

Data Availability Statement: Data will be made available on request.

Conflicts of Interest: Author Xiang Li was employed by the company Taizhou DongBo New Materials Co. Ltd. Author Kai Tang was employed by the company SINTEF Industry. The remaining authors declare that the research was conducted in the absence of any commercial or financial relationships that could be construed as a potential conflict of interest. The Taizhou DongBo New Materials Co. Ltd and SINTEF Industry had no role in the design of the study; in the collection, analyses, or interpretation of data; in the writing of the manuscript, or in the decision to publish the results.

References

1. Nitta, N.; Wu, F.; Lee, J.T.; Yushin, G. Li-ion battery materials: Present and future. *Mater. Today* **2015**, *18*, 252–264. [\[CrossRef\]](#)
2. Cui, Y. Silicon anodes. *Nat. Energy* **2021**, *6*, 995–996. [\[CrossRef\]](#)
3. Cheng, Z.; Jiang, H.; Zhang, X.; Cheng, F.; Wu, M.; Zhang, H. Fundamental Understanding and Facing Challenges in Structural Design of Porous Si-Based Anodes for Lithium-Ion Batteries. *Adv. Funct. Mater.* **2023**, *33*, 231109. [\[CrossRef\]](#)
4. Zhao, X.; Lehto, V.P. Challenges and prospects of nanosized silicon anodes in lithium-ion batteries. *Nanotechnology* **2021**, *32*, 042002. [\[CrossRef\]](#) [\[PubMed\]](#)
5. Wu, S.; Yu, B.; Wu, Z.; Fang, S.; Shi, B.; Yang, J. Effect of particle size distribution on the electrochemical performance of micro-sized silicon-based negative materials. *RSC Adv.* **2018**, *8*, 8544–8551. [\[CrossRef\]](#) [\[PubMed\]](#)
6. Lu, J.; Liu, J.; Gong, X.; Pang, S.; Zhou, C.; Li, H.; Qian, G.; Wang, Z. Upcycling of photovoltaic silicon waste into ultrahigh areal-loaded silicon nanowire electrodes through electrothermal shock. *Energy Storage Mater.* **2022**, *46*, 594–604. [\[CrossRef\]](#)
7. Ren, Y.; Xiang, L.; Yin, X.; Xiao, R.; Zuo, P.; Gao, Y.; Yin, G.; Du, C. Ultrathin Si Nanosheets Dispersed in Graphene Matrix Enable Stable Interface and High Rate Capability of Anode for Lithium-ion Batteries. *Adv. Funct. Mater.* **2022**, *32*, 2110046. [\[CrossRef\]](#)
8. Patil, R.; Phadatare, M.; Blomquist, N.; Örtengren, J.; Hummelgård, M.; Meshram, J.; Dubal, D.; Olin, H. Highly Stable Cycling of Silicon-Nanographite Aerogel-Based Anode for Lithium-Ion Batteries. *ACS Omega* **2021**, *6*, 6600–6606. [\[CrossRef\]](#) [\[PubMed\]](#)
9. Phadatare, M.; Patil, R.; Blomquist, N.; Forsberg, S.; Örtengren, J.; Hummelgård, M.; Meshram, J.; Hernández, G.; Brandell, D.; Leifer, K.; et al. Silicon-Nanographite Aerogel-Based Anodes for High Performance Lithium Ion Batteries. *Sci. Rep.* **2019**, *9*, 14621. [\[CrossRef\]](#) [\[PubMed\]](#)
10. Peng, J.; Li, W.; Wu, Z.; Li, H.; Zeng, P.; Chen, G.; Chang, B.; Zhang, X.; Wang, X. Si/C composite embedded nano-Si in 3D porous carbon matrix and enwound by conductive CNTs as anode of lithium-ion batteries. *Sustain. Mater. Technol.* **2022**, *32*, e00410. [\[CrossRef\]](#)
11. Guan, P.; Zhang, W.; Li, C.; Han, N.; Wang, X.; Li, Q.; Song, G.; Peng, Z.; Li, J.; Zhang, L.; et al. Low-cost urchin-like silicon-based anode with superior conductivity for lithium storage applications. *J. Colloid. Interface Sci.* **2020**, *575*, 150–157. [\[CrossRef\]](#) [\[PubMed\]](#)
12. He, S.; Huang, S.; Wang, S.; Mizota, I.; Liu, X.; Hou, X. Considering Critical Factors of Silicon/Graphite Anode Materials for Practical High-Energy Lithium-Ion Battery Applications. *Energy Fuels* **2020**, *35*, 944–964. [\[CrossRef\]](#)
13. Bai, M.; Yang, L.; Jia, Q.; Tang, X.; Liu, Y.; Wang, H.; Zhang, M.; Guo, R.; Ma, Y. Encasing Prelithiated Silicon Species in the Graphite Scaffold: An Enabling Anode Design for the Highly Reversible, Energy-Dense Cell Model. *ACS Appl. Mater. Interfaces* **2020**, *12*, 47490–47502. [\[CrossRef\]](#) [\[PubMed\]](#)

14. Ahuja, U.; Wang, B.; Hu, P.; Rethore, J.; Aifantis, K.E. Polydopamine coated Si nanoparticles allow for improved mechanical and electrochemical stability. *Electrochim. Acta* **2021**, *392*, 138993. [[CrossRef](#)]
15. Gueon, D.; Moon, J.H. Polydopamine-wrapped, silicon nanoparticle-impregnated macroporous CNT particles: Rational design of high-performance lithium-ion battery anodes. *Chem. Commun.* **2019**, *55*, 361–364. [[CrossRef](#)] [[PubMed](#)]
16. Li, W.; Peng, J.; Li, H.; Wu, Z.; Chang, B.; Guo, X.; Chen, G.; Wang, X. Architecture and performance of Si/C microspheres assembled by nano-Si via electro-spray technology as stability-enhanced anodes for lithium-ion batteries. *J. Alloys Compd.* **2022**, *903*, 163940. [[CrossRef](#)]
17. Zhao, F.; Zhao, M.; Dong, Y.; Ma, L.; Zhang, Y.; Niu, S.; Wei, L. Facile preparation of micron-sized silicon-graphite-carbon composite as anode material for high-performance lithium-ion batteries. *Powder Technol.* **2022**, *404*, 117455. [[CrossRef](#)]
18. Liu, X.; Wang, Z.; Guo, H.; Li, X.; Zhou, R.; Zhou, Y. Chitosan: A N-doped carbon source of silicon-based anode material for lithium ion batteries. *Ionics* **2017**, *23*, 2311–2318. [[CrossRef](#)]
19. Hou, S.-C.; Chen, T.-Y.; Wu, Y.-H.; Chen, H.-Y.; Lin, X.-D.; Liew, W.-K.; Chang, C.-C.; Huang, J.-L. Influence of Glucose Derivatives on Ball-Milled Si for Negative Electrodes with High Area Capacity in Lithium-Ion Batteries. *ACS Sustain. Chem. Eng.* **2019**, *7*, 2971–2979. [[CrossRef](#)]
20. Ensafi, A.A.; Abarghoui, M.M.; Rezaei, B. Metal (Ni and Bi) coated porous silicon nanostructure, high-performance anode materials for lithium ion batteries with high capacity and stability. *J. Alloys Compd.* **2017**, *712*, 233–240. [[CrossRef](#)]
21. Yu, Y.; Gu, L.; Zhu, C.; Tsukimoto, S.; Van Aken, P.A.; Maier, J. Reversible storage of lithium in silver-coated three-dimensional macroporous silicon. *Adv. Mater.* **2010**, *20*, 2247–2250. [[CrossRef](#)] [[PubMed](#)]
22. Wu, H.; Jiang, Y.; Liu, W.; Wen, H.; Dong, S.; Chen, H.; Su, L.; Wang, L. Engineering Bamboo Leaves Into 3D Macroporous Si@C Composites for Stable Lithium-Ion Battery Anodes. *Front. Chem.* **2022**, *10*, 882681. [[CrossRef](#)] [[PubMed](#)]
23. Zhang, F.; Zhu, W.; Li, T.; Yuan, Y.; Yin, J.; Jiang, J.; Yang, L. Advances of Synthesis Methods for Porous Silicon-Based Anode Materials. *Front. Chem.* **2022**, *10*, 889563. [[CrossRef](#)] [[PubMed](#)]
24. Zhang, Z.; Xi, F.; Li, S.; Wan, X.; Ma, W.; Chen, X.; Chen, Z.; Deng, R.; Ji, J.; Fan, H.-J.; et al. High-performance Si/nano-Cu/CNTs/C anode derived from photovoltaic silicon waste: A potential photovoltaic-energy storage strategy. *Mater. Today Energy* **2021**, *20*, 100671. [[CrossRef](#)]
25. Shi, H.; Zhang, W.; Wang, J.; Wang, D.; Wang, C.; Xiong, Z.; Wu, J.; Bai, Z.; Yan, X. Scalable synthesis of a porous structure silicon/carbon composite decorated with copper as an anode for lithium ion batteries. *Appl. Surf. Sci.* **2023**, *620*, 156843. [[CrossRef](#)]
26. Li, Y.; Chen, G.; Yang, H.; Geng, X.; Luo, Z.; Zhang, C.; Huang, L.; Luo, X. Three-Dimensional Porous Si@SiO_x/Ag/CN Anode Derived from Deposition Silicon Waste toward High-Performance Li-Ion Batteries. *ACS Appl. Mater. Interfaces* **2023**, *15*, 43887–43898. [[CrossRef](#)] [[PubMed](#)]
27. Yin, S.; Zhao, D.; Ji, Q.; Xia, Y.; Xia, S.; Wang, X.; Wang, M.; Ban, J.; Zhang, Y.; Metwalli, E.; et al. Si/Ag/C Nanohybrids with in Situ Incorporation of Super-Small Silver Nanoparticles: Tiny Amount, Huge Impact. *ACS Nano* **2018**, *12*, 861–875. [[CrossRef](#)]
28. Chou, C.-Y.; Kuo, J.-R.; Yen, S.-C. Silicon-Based Composite Negative Electrode Prepared from Recycled Silicon-Slicing Slurries and Lignin/Lignocellulose for Li-Ion Cells. *ACS Sustain. Chem. Eng.* **2018**, *6*, 4759–4766. [[CrossRef](#)]
29. Kong, J.; Xing, P.; Liu, Y.; Wang, J.; Jin, X.; Feng, Z.; Luo, X. An Economical Approach for the Recycling of High-Purity Silicon from Diamond-Wire Saw Kerf Slurry Waste. *Silicon* **2018**, *11*, 367–376. [[CrossRef](#)]
30. Li, X.; Lv, G.; Ma, W.; Li, T.; Zhang, R.; Zhang, J.; Li, S.; Lei, Y. Review of resource and recycling of silicon powder from diamond-wire sawing silicon waste. *J. Hazard. Mater.* **2022**, *424*, 127389. [[CrossRef](#)]
31. Liu, W.; Liu, J.; Zhu, M.; Wang, W.; Wang, L.; Xie, S.; Wang, L.; Yang, X.; He, X.; Sun, Y. Recycling of Lignin and Si Waste for Advanced Si/C Battery Anodes. *ACS Appl. Mater. Interfaces* **2020**, *12*, 57055–57063. [[CrossRef](#)] [[PubMed](#)]
32. Ji, H.; Xu, X.; Li, X.; Li, K.; Yuan, L.; Han, Z.; Tang, K. A low-cost Si@C composite for lithium-ion batteries anode materials synthesized via freeze-drying process using kerf loss Si waste. *Ionics* **2024**, *30*, 2585–2599. [[CrossRef](#)]
33. Wan, Y.; Yang, W.; Jin, C.; Shi, B.; Xu, G.; Yue, Z.; Li, Y.; Sun, F.; Zhou, L. Preparation of porous silicon by Ag-assisted chemical etching in non-filling type carbon shell for high performance lithium-ion batteries. *Solid. State Sci.* **2023**, *145*, 107329. [[CrossRef](#)]
34. Feng, Y.; Zhang, Y.; Song, Y.; Li, P.; Liu, J. Binary Carbon Modification Promoting the Electrochemical Performance of Silicon Anode for Lithium-Ion Batteries. *ChemistrySelect* **2023**, *8*, e202204086. [[CrossRef](#)]
35. Xi, F.; Zhang, Z.; Wan, X.; Li, S.; Ma, W.; Chen, X.; Chen, R.; Luo, B.; Wang, L. High-Performance Porous Silicon/Nanosilver Anodes from Industrial Low-Grade Silicon for Lithium-Ion Batteries. *ACS Appl. Mater. Interfaces* **2020**, *12*, 49080–49089. [[CrossRef](#)] [[PubMed](#)]
36. Xi, F.; Zhang, Z.; Hu, Y.; Li, S.; Ma, W.; Chen, X.; Wan, X.; Chong, C.; Luo, B.; Wang, L. PSi@SiO_x/Nano-Ag composite derived from silicon cutting waste as high-performance anode material for Li-ion batteries. *J. Hazard. Mater.* **2021**, *414*, 125480. [[CrossRef](#)] [[PubMed](#)]
37. Huang, Z.; Geyer, N.; Werner, P.; de Boor, J.; Gösele, U. Metal-Assisted Chemical Etching of Silicon: A Review. *Adv. Mater.* **2010**, *23*, 285–308. [[CrossRef](#)] [[PubMed](#)]
38. Eon Jun, S.; Choi, S.; Kim, J.; Kwon, K.C.; Park, S.H.; Jang, H.W. Non-noble metal single atom catalysts for electrochemical energy conversion reactions. *Chin. J. Catal.* **2023**, *50*, 195–214. [[CrossRef](#)]
39. Hou, X.; Zhang, M.; Wang, J.; Hu, S.; Liu, X. Deposition of silver nanoparticles into silicon/carbon composite as a high-performance anode material for Li-ion batteries. *J. Solid. State Electrochem.* **2015**, *19*, 3595–3604. [[CrossRef](#)]

40. Na, W.K.; Lim, H.M.; Huh, S.H.; Park, S.E.; Lee, Y.-S.; Lee, S.H. Effect of the average particle size and the surface oxidation layer of silicon on the colloidal silica particle through direct oxidation. *Mater. Sci. Eng. B* **2009**, *163*, 82–87. [[CrossRef](#)]
41. Zhang, Z.; Xi, F.; Ma, Q.; Wan, X.; Li, S.; Ma, W.; Chen, X.; Chen, Z.; Deng, R.; Ji, J.; et al. A nanosilver-actuated high-performance porous silicon anode from recycling of silicon waste. *Mater. Today Nano* **2022**, *17*, 100162. [[CrossRef](#)]
42. Wang, L.; Xi, F.; Zhang, Z.; Li, S.; Chen, X.; Wan, X.; Ma, W.; Deng, R.; Chong, C. Recycling of photovoltaic silicon waste for high-performance porous silicon/silver/carbon/graphite anode. *Waste Manag.* **2021**, *132*, 56–63. [[CrossRef](#)] [[PubMed](#)]
43. An, Y.; Tian, Y.; Wei, C.; Jiang, H.; Xi, B.; Xiong, S.; Feng, J.; Qian, Y. Scalable and Physical Synthesis of 2D Silicon from Bulk Layered Alloy for Lithium-Ion Batteries and Lithium Metal Batteries. *ACS Nano* **2019**, *13*, 13690–13701. [[CrossRef](#)] [[PubMed](#)]
44. Ji, H.; Liu, Z.; Li, X.; Li, J.; Yan, Z.; Tang, K. Recycling Silicon Waste from the Photovoltaic Industry to Prepare Yolk–Shell Si@void@C Anode Materials for Lithium–Ion Batteries. *Processes* **2023**, *11*, 1764. [[CrossRef](#)]
45. Tong, L.; Long, K.; Chen, L.; Wu, Z.; Chen, Y. High-Capacity and Long-Lived Silicon Anodes Enabled by Three-Dimensional Porous Conductive Network Design and Surface Reconstruction. *ACS Appl. Energy Mater.* **2022**, *5*, 13877–13886. [[CrossRef](#)]
46. Zhang, Z.; Ying, H.; Huang, P.; Zhang, S.; Zhang, Z.; Yang, T.; Han, W.-Q. Porous Si decorated on MXene as free-standing anodes for lithium-ion batteries with enhanced diffusion properties and mechanical stability. *Chem. Eng. J.* **2023**, *451*, 138785. [[CrossRef](#)]
47. He, Q.; Yu, J.; Wang, Y.; Zhong, Z.; Jiang, J.; Su, F. Silicon nanoparticles prepared from industrial wastes as high-performing anode materials for lithium ion batteries. *Solid. State Ion.* **2018**, *325*, 141–147. [[CrossRef](#)]
48. Huang, J.; Li, J.; Ye, L.; Wu, M.; Liu, H.; Cui, Y.; Lian, J.; Wang, C. Synthesis of Si/C Composites by Silicon Waste Recycling and Carbon Coating for High-Capacity Lithium-Ion Storage. *Nanomaterials* **2023**, *13*, 2142. [[CrossRef](#)] [[PubMed](#)]
49. Kang, W.; Kim, J.-C.; Kim, D.-W. Waste glass microfiber filter-derived fabrication of fibrous yolk-shell structured silicon/carbon composite freestanding electrodes for lithium-ion battery anodes. *J. Power Sources* **2020**, *468*, 228407. [[CrossRef](#)]
50. Ren, W.; Zhang, Z.; Wang, Y.; Tan, Q.; Zhong, Z.; Su, F. Preparation of porous silicon/carbon microspheres as high performance anode materials for lithium ion batteries. *J. Mater. Chem. A* **2015**, *3*, 5859–5865. [[CrossRef](#)]
51. Wang, K.; Xue, B.; Tan, Y.; Sun, J.; Li, Q.; Shi, S.; Li, P. Recycling of micron-sized Si powder waste from diamond wire cutting and its application in Li-ion battery anodes. *J. Clean. Prod.* **2019**, *239*, 117997. [[CrossRef](#)]
52. Xiang, K.; Wang, X.; Chen, M.; Shen, Y.; Shu, H.; Yang, X. Industrial waste silica preparation of silicon carbide composites and their applications in lithium-ion battery anode. *J. Alloys Compd.* **2017**, *695*, 100–105. [[CrossRef](#)]
53. Yang, T.; Gao, Y.; Tang, Y.; Zhang, Y.; Li, X.; Liu, L. Porous silicon from industrial waste engineered for superior stability lithium-ion battery anodes. *J. Nanopart. Res.* **2021**, *23*, 209. [[CrossRef](#)]
54. Zhang, Y.; Chen, M.; Chen, Z.; Wang, Y.; Li, S.; Duan, P.; Zhong, Y.; Wu, Z.; Guo, X.; Yan, Z.; et al. Constructing cycle-stable Si/TiSi₂ composites as anode materials for lithium ion batteries through direct utilization of low-purity Si and Ti-bearing blast furnace slag. *J. Alloys Compd.* **2021**, *876*, 160125. [[CrossRef](#)]
55. An, Y.; Tian, Y.; Liu, C.; Xiong, S.; Feng, J.; Qian, Y. One-Step, Vacuum-Assisted Construction of Micrometer-Sized Nanoporous Silicon Confined by Uniform Two-Dimensional N-Doped Carbon toward Advanced Li Ion and MXene-Based Li Metal Batteries. *ACS Nano* **2022**, *16*, 4560–4577. [[CrossRef](#)] [[PubMed](#)]
56. Xu, Z.; Zheng, E.; Xiao, Z.; Shao, H.; Liu, Y.; Wang, J. Photo-Initiated in situ synthesis of polypyrrole Fe-Coated porous silicon microspheres for High-performance Lithium-ion battery anodes. *Chem. Eng. J.* **2023**, *459*, 141543. [[CrossRef](#)]
57. Augustyn, V.; Come, J.; Lowe, M.A.; Kim, J.W.; Taberna, P.L.; Tolbert, S.H.; Abruña, H.D.; Simon, P.; Dunn, B. High-rate electrochemical energy storage through Li⁺ intercalation pseudocapacitance. *Nat. Mater.* **2013**, *12*, 518–522. [[CrossRef](#)] [[PubMed](#)]
58. Xia, M.; Chen, B.; Gu, F.; Zu, L.; Xu, M.; Feng, Y.; Wang, Z.; Zhang, H.; Zhang, C.; Yang, J. Ti₃C₂T_x MXene Nanosheets as a Robust and Conductive Tight on Si Anodes Significantly Enhance Electrochemical Lithium Storage Performance. *ACS Nano* **2020**, *14*, 5111–5120. [[CrossRef](#)] [[PubMed](#)]
59. Zhang, W.; Shi, H.; Wang, D.; Wang, J.; Xiong, Z.; Wang, C.; Gu, Y.; Bai, Z.; Liang, Q.; Yan, X. Three-dimensional Ti₃C₂ MXene@silicon@nitrogen-doped carbon foam for high performance self-standing lithium-ion battery anodes. *J. Electroanal. Chem.* **2022**, *921*, 116664. [[CrossRef](#)]

Disclaimer/Publisher’s Note: The statements, opinions and data contained in all publications are solely those of the individual author(s) and contributor(s) and not of MDPI and/or the editor(s). MDPI and/or the editor(s) disclaim responsibility for any injury to people or property resulting from any ideas, methods, instructions or products referred to in the content.